

Optical constants, band gap, and infrared-active phonons of $(\text{LaAlO}_3)_{0.3}(\text{Sr}_2\text{AlTaO}_6)_{0.35}$ (LSAT) from spectroscopic ellipsometry

Timothy Nathan Nunley, Travis I. Willett-Gies, and Jacqueline A. Cooke

Department of Physics, New Mexico State University, MSC 3D, P.O. Box 30001, Las Cruces, New Mexico 88003-8001

Felicia S. Manciu

Department of Physics, University of Texas at El Paso, El Paso, Texas 79968

Premysl Marsik and Christian Bernhard

Department of Physics and Fribourg Center for Nanomaterials, University of Fribourg, Chemin du Musee 3, CH-1700 Fribourg, Switzerland

Stefan Zollner^{a)}

Department of Physics, New Mexico State University, MSC 3D, P.O. Box 30001, Las Cruces, New Mexico 88003-8001

Using spectroscopic ellipsometry, the authors determined the optical constants (complex dielectric function) for $(\text{LaAlO}_3)_{0.3}(\text{Sr}_2\text{AlTaO}_6)_{0.35}$ (LSAT) from 0.01 to 6.5 eV. Above 0.5 eV, the data were described with a sum of two Tauc-Lorentz oscillators and two poles. A direct gap of 5.8 ± 0.1 eV was found. An Urbach tail extends to even lower photon energies and makes the crystal opaque above 4.8 eV. Using Fourier-transform infrared ellipsometry, the lattice dynamics was studied. Nine pairs of transverse/longitudinal phonons were found and attributed to disorder in the La/Sr sublattice, ordering in the Al/Ta sublattice, and two-phonon absorption.

I. INTRODUCTION

Perovskite oxides like SrTiO_3 and related compounds with a generic formula ABO_3 have interesting properties, such as ferroelectricity, superconductivity, high dielectric constants, combined with a large band gap, which may lead to interesting electronic, optoelectronic, or energy-conversion applications.¹ These properties can often be tuned by strain engineering,² which requires epitaxial growth on a variety of substrates with different lattice constants.³

One common perovskite substrate material has the chemical formula $(\text{LaAlO}_3)_{0.3}(\text{Sr}_2\text{AlTaO}_6)_{0.35}$ (LSAT), equivalent to $(\text{La}_{0.3}\text{Sr}_{0.7})(\text{Al}_{0.65}\text{Ta}_{0.35})\text{O}_3$, which is usually abbreviated as LSAT. It has been used as a substrate for epitaxial growth⁴⁻⁷ of PbVO_3 , EuTiO_3 , NbO_2 , NaNbO_3 , and many other materials. Unlike LaAlO_3 (another common substrate, which has a rhombohedral crystal structure⁸), LSAT is cubic. LSAT substrates therefore are untwinned and allow higher quality epitaxial growth than commercial twinned (pseudocubic) LaAlO_3 substrates. The cubic structure leads to an isotropic dielectric function.

LSAT is usually treated as a simple cubic (SC) perovskite at room temperature⁹ with space group $\text{Pm}\bar{3}\text{m}$ (221) and a lattice constant $a = 3.868$ Å, consistent with random occupation of the A (La/Sr) and B (Al/Ta) sites. On the other hand, ordering at the Al/Ta sites,^{10,11} similar to $\text{Sr}_2\text{AlTaO}_6$, leads to a face-centered cubic (FCC) crystal structure with a lattice constant of $a = 7.73$ Å and an $\text{F}\bar{4}3\text{m}$ (216) space group. Sublattice disorder or ordering will affect the phonon symmetries in the crystal.¹² Some crystals have both ordered and disordered domains.¹⁰

Spectroscopic ellipsometry¹³⁻¹⁶ is an important technique to characterize epitaxial films on a substrate and allows conclusions about the electronic and vibrational structure of epitaxial materials. Therefore, the detailed and precise knowledge of the dielectric function of LSAT is crucial. In this article, we present new information about the optical constants of LSAT and about its electronic and vibrational properties.

Previous studies of the dielectric function ϵ of LSAT and its electronic and vibrational properties have been limited. Transmission measurements^{17,18} established the absorption edge (near 260 nm) and a broad defect absorption band near 450 nm, responsible for the color of the crystal, which depended on annealing conditions. The refractive index $n = \sqrt{\epsilon}$ in the transparent region was determined using the minimum-deviation prism method¹⁸ and by spectroscopic ellipsometry³ and fitted with the Sellmeier equation.

The zone-center phonons were studied using infrared reflectance,^{12,19} far-infrared ellipsometry,²⁰ and Raman spectroscopy.¹² The symmetries of these phonons for the two possible (ordered and disordered) space groups were also identified.¹²

II. EXPERIMENT AND MODELS

Czochralski-grown LSAT wafers with colorless to light brown appearance and (100) surface orientation (less than 0.5° miscut) were obtained commercially (MTI Corporation, Richmond, CA). Single-side polished wafers were used for spectroscopic ellipsometry and infrared ellipsometry from 0.8 to 6.5 eV and 0.03 to 0.7 eV, respectively, while transmission measurements were performed on two-side polished

^{a)}Electronic mail: zollner@nmsu.edu

wafers with 0.5 mm thickness. The surface roughness was specified by the supplier to be below 8 Å.

Figure 1(a) shows a symmetric $\omega/2\theta$ x-ray diffraction (XRD) scan for the LSAT (100) substrate obtained with Cu $K_{\alpha 1,2}$ radiation on a PANalytical Empyrean diffractometer. Miller indices are marked in the SC notation, where all (hkl) reflections are allowed. The lattice constant was determined to be 3.870 ± 0.002 Å. The FWHM of the (200) rocking curve (ω scan at fixed 2θ value), obtained with a hybrid monochromator, was 0.05° . This is larger than for a Si (100) substrate (FWHM = 0.01°), but significantly smaller than for a twinned LaAlO_3 substrate, allowing better alignment of epitaxial films on LSAT than on LaAlO_3 .

In the double perovskite (ordered) FCC structure of $\text{Sr}_2\text{AlTaO}_6$, the Miller indices are doubled relative to the SC perovskite structure, but the FCC (hkl) indices must all be either even or odd for allowed reflections. Therefore, all $(h00)$ SC reflections in a symmetric $\omega/2\theta$ scan as shown in Fig. 1(a) are also allowed in the FCC structure, where we would denote them as $(2h00)$. To show evidence of ordering, we must look for FCC (hkl) reflections with odd indices, since these are equivalent to (forbidden) half-integral Miller indices in the SC structure.¹⁰ This requires asymmetric reflections for an LSAT (100) surface.

We indeed find strong FCC (115), (117), and (555) Bragg reflections as clear evidence of ordering in our sample. Figure 1(c) shows a ϕ scan of the FCC (115) Bragg reflection, where the sample is rotated about its surface normal for fixed incidence and diffraction angles satisfying the (115) Bragg condition. The four-fold symmetry of the (100) surface is apparent in the ϕ -scan. The (115) Bragg peak has a rather large 2θ half-width of 0.6° , which corresponds to an approximate size of 15 nm for the ordered domains, if the Scherrer formula is applied. This domain size is consistent

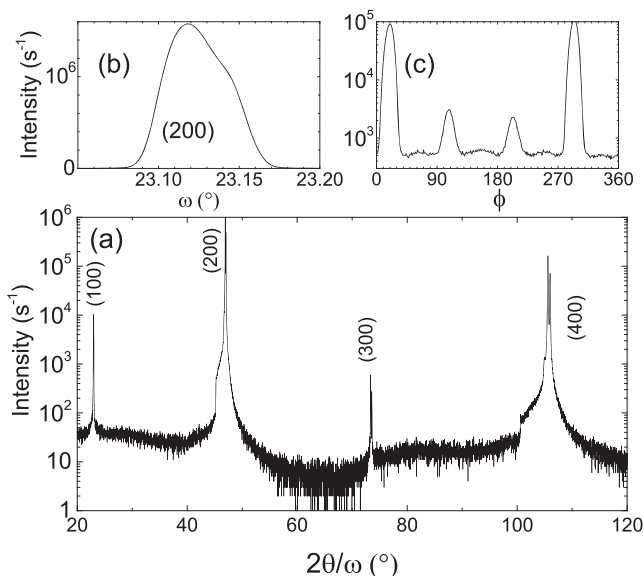


FIG. 1. (a) Symmetric $2\theta/\omega$ x-ray diffraction scan for an LSAT wafer with (100) orientation. Miller indices are indicated in the simple cubic perovskite notation. (b) Rocking curve for the (200) Bragg reflection with a FWHM of 0.05° . (c) ϕ -scan of the (115) Bragg reflection of the ordered FCC LSAT structure.

with previous XRD and transmission electron microscopy of LSAT.¹⁰

Raman measurements were performed at 300 K in a back-scattering geometry with an alpha 300R WITec system, using the 532 nm excitation of a Nd:YAG laser and a 20× objective lens with a numerical aperture of 0.4. The complete Raman spectrum was acquired from an accumulation of ten scans, with each scan at an integration time of 50 ms. The Raman signal was detected by a 1024×127 pixel Peltier cooled CCD camera with a spectral resolution of 4 cm^{-1} .

Prior to the ellipsometry measurements, wafers were cleaned in a Novascan PSD Pro series digital UV ozone system utilizing a Hg vapor lamp. The purpose of this cleaning is to remove organic contamination from the surface. It was performed in an oxygen-enriched environment for 30 min with the Hg lamp on and the sample on a heating stage held at 150°C , followed by a 30-min period of incubation with the lamp off and the sample cooling to room temperature.

The ellipsometric angles ψ and Δ from 0.8 to 6.5 eV were determined at 300 K in air on a J. A. Woollam vertical variable-angle spectroscopic ellipsometer with computer controlled Berek waveplate compensator (J.A. Woollam Co, Lincoln, NE). We selected angles of incidence ϕ between 60° and 80° . The same instrument was also used to perform transmission measurements at normal incidence, using a measurement without sample as the reference. In the midinfrared spectral region from 250 to 8000 cm^{-1} , ψ and Δ were acquired at 300 K on a J.A. Woollam Fourier-transform infrared (FTIR) ellipsometer as described elsewhere.^{8,21,22} We also merged our data with far-infrared ellipsometry²³ results taken for a different sample (obtained from Crystec GmbH, Berlin, Germany) at $\phi = 75^\circ$ from 80 to 650 cm^{-1} presented previously.²⁰ There is excellent agreement between the far-infrared and midinfrared data in the region of overlap.

The ellipsometric angles are influenced by the surface conditions of the sample, which include surface roughness and overlayers, especially organic contaminants. Therefore, it is desirable to reduce the surface layer thickness as much as possible. A roughness correction using the Bruggeman effective medium approximation with a 50/50 mixture of LSAT and voids allows to consider the remaining surface effects numerically. To describe the large ellipsometry data set, it is convenient to represent the dispersion of LSAT with parametric models. The Sellmeier equation and the Tauc-Lorentz model have been particularly useful. The parameters governing the dispersion and the surface roughness layer thickness are adjusted to minimize the deviation between the data and the fit, weighted by the experimental errors in the data. These technical details are well described in ellipsometry textbooks^{13–16} and our prior research^{8,21,22} on NiO and LaAlO_3 .

III. RESULTS FROM NEAR-IR TO UV AT 300 K

The transmission through a two-side polished LSAT substrate with 0.5 mm thickness is shown in Fig. 2 (dashed). Since the refractive index $n = 1.99$ at 1 eV (see below), the reflection loss at each surface is 11%, leading to a transmission of 79%

in the absence of absorption, consistent with the measured transmission in Fig. 2.

The absorption coefficient α can be calculated from the transmission, if the thickness of the sample (0.5 mm) and the dispersion of the refractive index (see below) are known.²⁴ Results are shown in Fig. 2 (solid). The absorption coefficient is very small at low energies (not measurable) and rises sharply between 4.6 and 4.8 eV (260 nm), near the fundamental absorption gap of LSAT, as reported previously.¹⁷ The position of this absorption edge depends on the thickness of the sample and details of the instrumentation. Our transmission measurements are unable to determine if this band gap is direct or indirect.

There is also a minimum in the transmission and a peak in the absorption coefficient near 410 nm (3.0 eV). This absorption band has been seen previously¹⁷ and can be reduced by annealing at 1650 °C in Ar with a trace of hydrogen. Presumably, it is due to defects, not related to the bulk electronic band structure. A similar absorption band within the gap was found in SiC, where it was explained by inter-conduction band transitions.²⁵

The ellipsometric angles ψ and Δ taken at angles of incidence between 60° and 80° are shown in Fig. 3 (symbols). The depolarization was small (below 1% throughout the spectral range) and not related to the sample. Since LSAT is transparent throughout the visible, a Cauchy fit gives an excellent description of the data, if a surface roughness layer (described using the Bruggeman effective medium theory as a 50/50 mixture of LSAT and voids) of 19.1 Å thickness is considered. The S-like transition of Δ from 0° to 180° near the Brewster angle (between 64° and 70°, depending on the photon energy) is most sensitive to surface roughness. Therefore, measuring at many incidence angles is helpful to accurately determine the surface roughness layer thickness.

A good description of the data between 0.8 and 6 eV can be achieved using a single Tauc-Lorentz oscillator, with poles at 0.08 eV (fixed) and 11.556 eV (variable) to take into account dispersion from absorption peaks outside of our spectral range. The agreement can be improved slightly, especially above 6 eV, if a second Tauc-Lorentz oscillator is

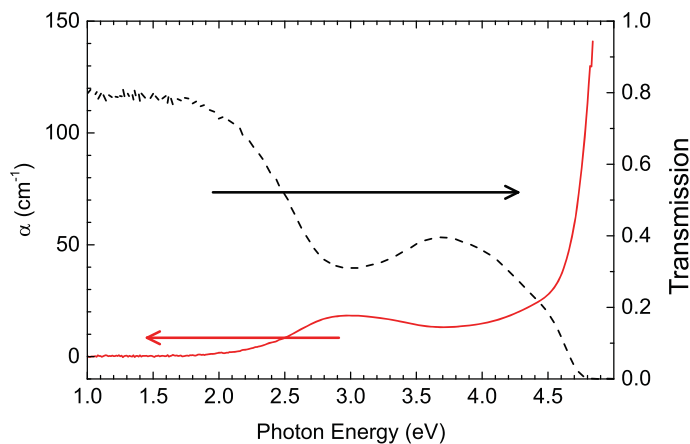


FIG. 2. (Color online) Transmission (dashed) and absorption coefficient (solid) for a two-side polished LSAT wafer with 0.5 mm thickness obtained at 300 K from a normal-incidence transmission measurement.

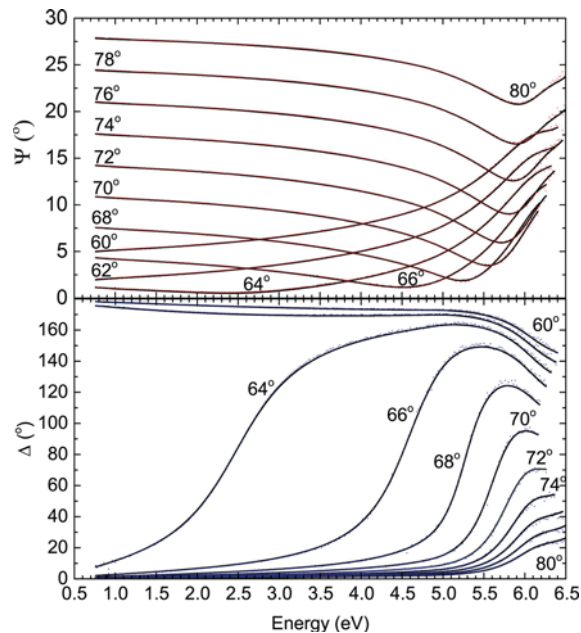


FIG. 3. (Color online) Ellipsometric angles ψ and Δ vs photon energy for incidence angles from 60° to 80° (symbols) for LSAT at 300 K. The lines show a fit with two poles and two Tauc-Lorentz oscillators, assuming a surface roughness of 19.1 Å.

added. The best fit to the data with two Tauc-Lorentz oscillators is shown by solid lines in Fig. 3. The Tauc-Lorentz and pole parameters obtained from the fit are shown in Table I. In both cases, the rms deviation between fit and data is about 50% larger than the experimental errors.

The experimental data and fit are also displayed as a pseudo-dielectric function $\langle \epsilon \rangle$ in Fig. 4. The pseudoabsorption below the band gap due to surface roughness is clearly visible.

Finally, we show the dielectric function of LSAT from our model with two Tauc-Lorentz oscillators in Fig. 5 (solid). Agreement with previous data (dashed, dashed-dotted) is good,^{3,18} but our data cover a much broader spectral range. By extrapolating the dielectric constant toward zero energy (but subtracting the IR pole due to lattice absorption), we find the electronic contribution to the dielectric constant

TABLE I. Tauc-Lorentz (TL) parameters energy E , broadening Γ , amplitude A , and Tauc gap E_g for describing the dielectric function of LSAT at 300 K from 0.8 to 6.5 eV with one or two TL oscillators, obtained by fitting the parameters to the data in Fig. 3. The IR and UV pole energies and amplitudes are also listed. Probable errors are given in parentheses. (f) indicates that the parameter was fixed.

| No. | E (eV) | A | Γ (eV) | E_g (eV) |
|---------|----------|--------------------------|---------------|------------|
| TL1 | 6.292(7) | 126(2) eV | 1.21(2) | 5.007(9) |
| UV pole | 11.56(4) | 272(2) eV ² | | |
| IR pole | 0.08(f) | 0.026(1) eV ² | | |
| TL1 | 6.14(2) | 53(6) eV | 0.84(3) | 4.87(1) |
| TL2 | 6.67(4) | 38(7) eV | 0.7(1) | Same |
| UV pole | 11.56(4) | 289(2) eV ² | | |
| IR pole | 0.08(f) | 0.027(1) eV ² | | |

to be $\epsilon_\infty = 4.0$. (This is also known as the high-frequency dielectric constant, for frequencies much higher than those of lattice vibrations.)

To estimate the lowest direct band gap, we plot α^2 (determined from the ellipsometry data) versus photon energy in Fig. 6. An extrapolation to zero yields a direct band gap of 5.8 ± 0.1 eV, as shown by the dashed line. This direct band gap is significantly larger than the onset of absorption (between 4.6 and 4.8 eV, see Fig. 2) and the Tauc gap (4.9–5.0 eV, see Table I).

The onset of absorption is more clearly seen by plotting α on a semilogarithmic scale, shown by the inset in Fig. 6. The symbols show α determined from a wavelength-by-wavelength fit using a fixed surface layer thickness of 19.1 Å. We note that transmission measurements show $\alpha = 60$ cm⁻¹ at 4.7 eV (see Fig. 2), while our ellipsometry measurements find $\alpha \sim 500$ cm⁻¹. We add our usual warning that our ellipsometry setup is unable to determine α below 10^3 cm⁻¹. Smaller values of α are better measured in transmission.

IV. FAR-IR, MID-IR, AND RAMAN RESULTS

Our two-side polished LSAT wafer with 0.5 mm thickness is completely opaque in far-infrared FTIR transmission measurements from 70 to 1090 cm⁻¹, indicating strong lattice absorption. Raman spectra for LSAT (100) at 300 K are

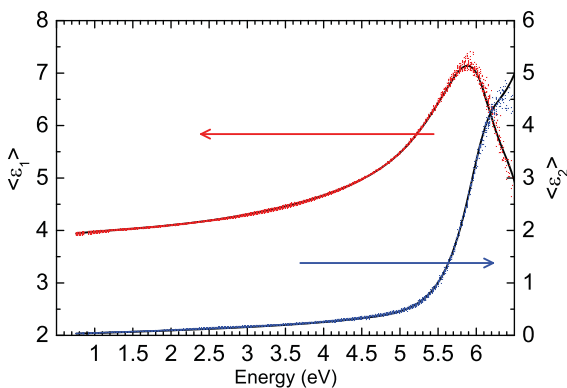


FIG. 4. (Color online) Same data as in Fig. 3, but displayed as a pseudodielectric function.

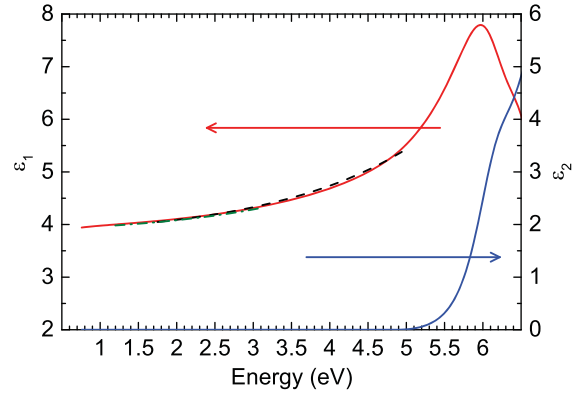


FIG. 5. (Color online) Real and imaginary part of the dielectric function ϵ of LSAT at 300 K described with two Tauc-Lorentz oscillators and two poles (solid), calculated using the parameters in Table I. Data calculated from the Sellmeier parameters listed in Ref. 3 (dashed) and Ref. 18 (dotted-dashed) are shown for comparison.

shown in Fig. 7. These LSAT spectra are similar to those reported in Ref. 12. As in the ordered double perovskite^{26,27} compound Sr₂AlTaO₃, four strong peaks are seen at 152 cm⁻¹ (T_{2g}), 471 cm⁻¹ (T_{2g}), 599 cm⁻¹ (E_g), and 883 cm⁻¹ (A_{1g}). Weaker peaks appear at 195, 425, and 735 cm⁻¹.

FTIR ellipsometry was used to investigate the lattice vibrations of LSAT at 300 K. The ellipsometric angles from 250 to 1400 cm⁻¹ for incidence angles ϕ from 65° to 75° are shown in Fig. 8. We also include far-infrared ellipsometry data from 80 to 650 cm⁻¹ at $\phi = 75^\circ$ published previously.²⁰ Only normal dispersion is found at larger energies. At 0.8 eV, the data merge seamlessly with those shown in Fig. 3. The same data are also shown as a pseudodielectric function in Fig. 9 and as a loss function in Fig. 10. Since surface roughness contributes negligibly in the far- and mid-IR, we do not distinguish between ϵ and $\langle \epsilon \rangle$ in this spectral range.

Infrared-active transverse optical (TO) phonons at the center of the Brillouin zone cause peaks in ϵ_2 due to infrared lattice absorption. For an ideal perovskite ABO₃, there are three IR active modes with T_{1u} symmetry. A fourth IR-active mode

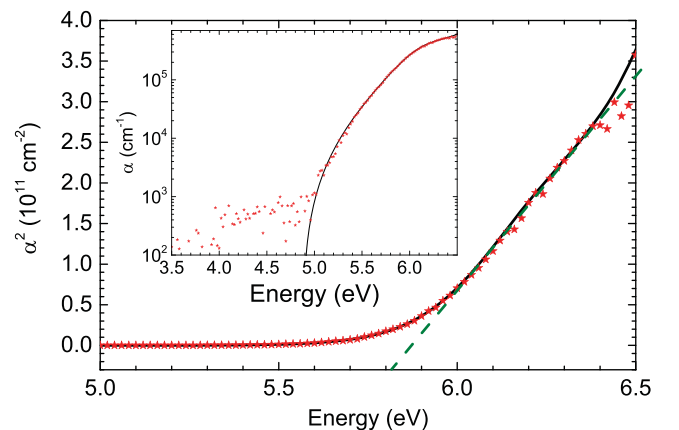


FIG. 6. (Color online) Square of the absorption coefficient of LSAT vs photon energy at 300 K can be extrapolated to yield a direct band gap of 5.8 ± 0.1 eV, as shown by the dashed line. Symbols were determined by direct inversion of the ellipsometric angles (wavelength-by-wavelength fit), while the solid line shows the result of the Tauc-Lorentz model. The inset shows α on a logarithmic scale.

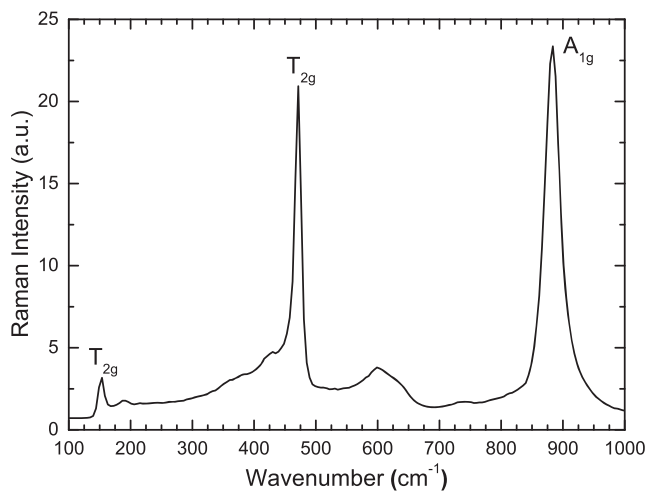


FIG. 7. Raman spectra for LSAT (100) at 300 K show four strong peaks, similar to $\text{Sr}_2\text{AlTaO}_6$. Symmetry assignments for the vibrations were taken from the literature (Refs. 12 and 27).

appears due to ordering at the Al/Ta sites, as in the double perovskite compound $\text{Sr}_2\text{AlTaO}_3$.¹² Additional modes are expected for random alloys, such as $\text{Si}_{1-x}\text{Ge}_x$,²⁸ or due to two-phonon absorption.²²

Since $(\text{La}_{0.3}\text{Sr}_{0.7})(\text{Al}_{0.65}\text{Ta}_{0.35})\text{O}_3$ has random occupation at both the A and B sites, we might expect up to 12 phonon modes, because each combination of La/Al, Sr/Al, La/Ta,

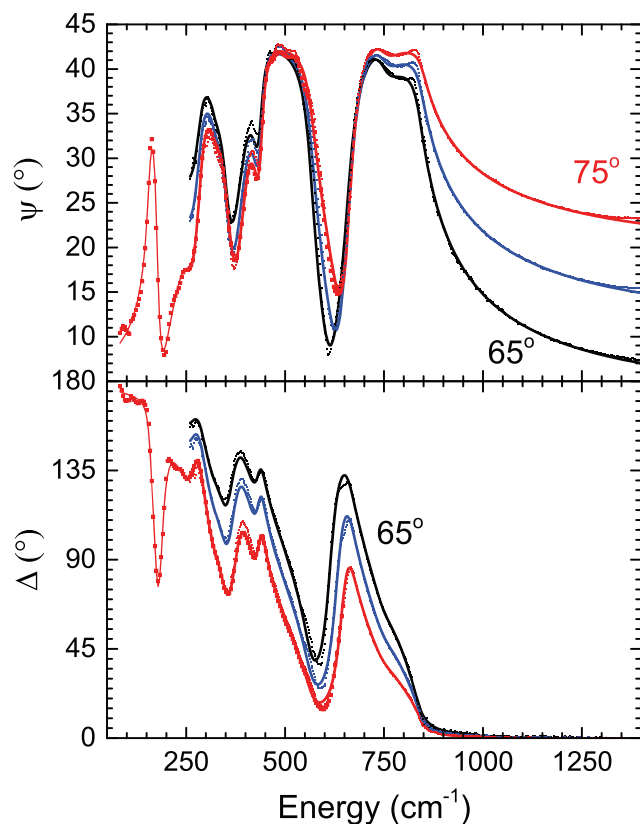


FIG. 8. (Color online) Ellipsometric angles ψ and Δ for LSAT at 300 K in the region of lattice absorption (symbols) for three angles of incidence (65° to 75°) in comparison with a fit to a factorized model with nine TO/LO phonon pairs (solid).

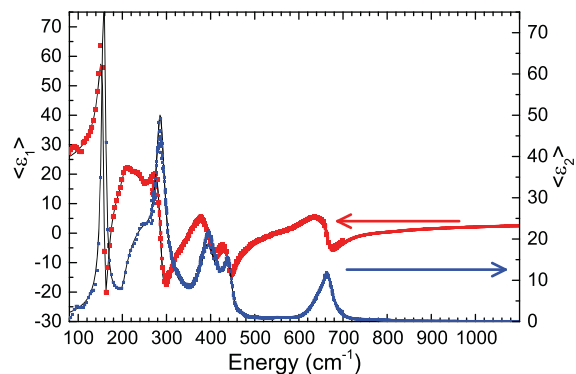


FIG. 9. (Color online) Same data as in Fig. 8, but shown as a pseudodielectric function.

and Sr/Ta might be associated with three T_{1u} phonons in the disordered perovskite phase. We find experimentally that only the La/Sr disorder contributes an additional strong phonon, for a total of five strong IR-active phonons, which appear as ϵ_2 peaks in Fig. 9. They are located approximately at 158, 286, 392, 442, and 666 cm^{-1} . Two weaker peaks exist between 220 and 250 cm^{-1} and another one at 330 cm^{-1} . A ninth phonon is needed to describe the dip in the ψ reststrahlen band near 790 cm^{-1} . In analogy to LiF and NiO, we assign this peak to two-phonon absorption.²²

Describing ϵ as a sum of Lorentzians²¹ allows us to estimate the energies, amplitudes, and broadenings of all nine TO phonons. Adding all amplitudes to the high-frequency dielectric constant $\epsilon_\infty = 4.0$ (see above), we find $\epsilon_s = 22.2 \pm 0.7$ for the static dielectric constant, in excellent agreement with the literature.^{29,30} Lorentz parameters for all phonons are shown in Table II. While an expansion of the dielectric function into such a large number of Lorentzians may seem somewhat arbitrary, we confirmed with far-IR measurements of LSAT at 10 K, that all Lorentzians used in our expansion are associated with peaks in ϵ_2 .

Describing infrared ellipsometry data with a sum of Lorentzians is expected to yield good agreement, if the individual TO phonons are well separated. For LSAT, the broadenings are larger than the phonon separations for some modes and therefore the agreement of the Lorentz model to the dielectric function is not perfect, just like for other materials such as LaAlO_3 , LiF, or NiO.^{21,22} The rms deviation

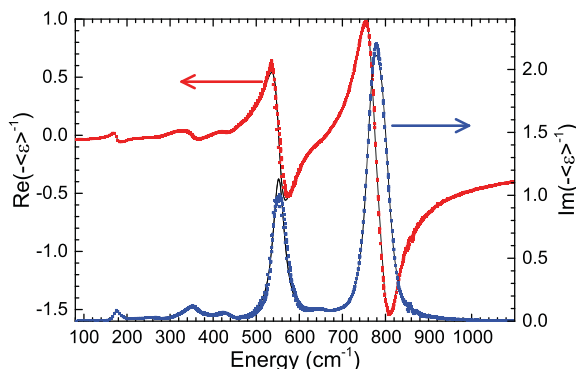


FIG. 10. (Color online) Same data as in Fig. 8, but shown as a pseudoloss function $-1/\langle \epsilon \rangle$.

TABLE II. Parameters for TO and LO phonons from FTIR ellipsometry: energy E , amplitude A , and broadening Γ . The top portion shows the parameters for nine Lorentz oscillators. The bottom portion describes ϵ with a product of nine LST factors for TO/LO phonon pairs. The LST amplitudes were calculated from Eq. (1).

| No. | A | E_{TO} (cm^{-1}) | Γ_{TO} (cm^{-1}) | E_{LO} (cm^{-1}) | Γ_{LO} (cm^{-1}) | Assignment |
|-----|-----------|---|--|---|--|--------------------|
| L1 | 6.30(4) | 156.9(1) | 12.8(3) | | | |
| L2 | 1.5(4) | 222(2) | 35(3) | | | |
| L3 | 2.6(5) | 248(1) | 42(6) | | | |
| L4 | 4.3(2) | 285.9(3) | 28(1) | | | |
| L5 | 0.46(8) | 330(2) | 46(6) | | | |
| L6 | 1.89(4) | 395.0(2) | 44(1) | | | |
| L7 | 0.51(2) | 436.4(2) | 18.6(7) | | | |
| L8 | 0.646(2) | 659.8(1) | 36.5(3) | | | |
| L9 | 0.0045(6) | 787(1) | 26(4) | | | |
| 1 | 5.58 | 158.1(1) | 10.7(2) | 174.1(1) | 14.7(2) | La-BO ₆ |
| 2 | 2.35 | 286.3(2) | 22.8(5) | 355.5(3) | 50.6(6) | Sr-BO ₆ |
| 3 | 1.56 | 392.3(3) | 40.5(5) | 432.0(5) | 43(1) | B-O bend |
| 4 | 0.43 | 442.1(2) | 22.4(4) | 552.5(2) | 33.1(4) | B-O bend |
| 5 | 0.11 | 632(1) | 46(2) | 638(2) | 58(3) | B-O stretch |
| 6 | 0.49 | 666.2(3) | 32.4(5) | 766.8(8) | 45.7(2) | B-O stretch |
| 7 | 0.01 | 789(2) | 74(5) | 800(1) | 48(2) | Two-phonon |
| 8 | -0.74 | 201.7(5) | 23(1) | 199(1) | 23(1) | |
| 9 | 9.50 | 251(1) | 115(3) | 277(1) | 57(2) | |

between data and model is about 5–10 times larger than the experimental errors. Nevertheless, this model is instructive, because it quickly yields phonon energies and amplitudes.

To improve the agreement between our model and the experiment, we write ϵ as a product of Lyddane–Sachs–Teller (LST) factors.²¹ As a starting point for our fit, we use the TO energies in Table II and the LO energies found from the peaks in the loss function in Fig. 10, i.e., 180, 350, 430, 550, and 780 cm^{-1} . The highest energy phonon has an asymmetric ϵ_2 lineshape. We therefore add a sixth TO/LO phonon pair to our model. The need for this phonon is also obvious from the inspection of the ψ reststrahlen band, which has a minimum near 770 cm^{-1} , demonstrating the presence of another phonon. Another three weak or broad TO/LO phonon pairs (7–9) are added to improve the fit for asymmetric peaks. A model with nine LST factors and the parameters shown in Table II gives very good agreement with the experiment, with the average rms deviation only six times larger than the experimental errors.

In general, there is no one-to-one correspondence between TO phonons in the Lorentz model and the LST model. However, we find that the strongest TO modes in the Lorentz model with the lowest broadening parameters also result in LST TO modes with similar frequencies, with differences up to a few wavenumbers. The same is not true for weaker or broader TO phonons.

We find one nonphysical LST factor with switched LO and TO energies, which is needed to describe the line shape around 200 cm^{-1} . Our results are in qualitative agreement with FTIR transmission measurements on LSAT crystals,¹² where five TO phonons were found at energies similar to

ours. We would like to note that there are sample to sample variations in phonon amplitudes that are dependent upon sample source and annealing treatment before measurement.

The phonon amplitudes can also be calculated from the factorized phonon model with³¹

$$A_j = \epsilon_\infty \frac{E_{j\text{LO}}^2 - E_{j\text{TO}}^2}{E_{j\text{TO}}^2} \prod_{k \neq j} \frac{E_{k\text{LO}}^2 - E_{j\text{TO}}^2}{E_{k\text{TO}}^2 - E_{j\text{TO}}^2}, \quad (1)$$

where the indices j and k label the TO/LO phonon pairs. The results listed in Table II show good agreement between the Lorentz and LST amplitudes for some modes and significant differences for others. Most importantly, the amplitude for the inverted TO/LO pair³⁴ at 202/199 cm^{-1} is negative. The high frequency dielectric constant is found to be $\epsilon_\infty = 3.96$. Using this and the calculated phonon amplitudes, the static dielectric constant calculated from our LST model is found to be approximately 23.25, which is still in good agreement with the experimental value.

Since only three TO phonon modes are expected for a perfect cubic perovskite ABO₃ and four modes for the (ordered) double perovskite Sr₂AlTaO₆,¹² we conclude that several of the phonons found in our model must be due to alloy disorder. The broad phonon at 765 cm^{-1} might be due to two-phonon absorption.

We assign our observed LSAT frequencies based on vibrational modes^{32–34} identified for cubic LaAlO₃: The lowest-energy modes (1–2) are vibrations of the (Al/Ta)O₆ octahedra against the La/Sr sublattice. The La-AlO₆ vibration in LaAlO₃ has energy of 190 cm^{-1} , which should be reduced by substituting Al with Ta. Also, the Sr-AlO₆ vibration should have a higher energy and therefore is identified with mode (2). Because of their large mass, it is not likely that the La/Sr sublattice participates in any of the modes at higher energies.³⁴ Similarly, the highest energy strong mode (5) at 666 cm^{-1} is an (Al/Ta)-O stretching mode, with the La/Sr sublattice immobile. The two intermediate modes (3–4) are (Al/Ta)-O bending modes. This mode is doubled because of ordering of the Al/Ta sublattice. The additional weak modes (7–9) are due to defects and disorder.

V. SUMMARY

We have used spectroscopic ellipsometry, FTIR ellipsometry, and Raman spectroscopy to characterize the electronic and vibrational properties of LSAT from 0.01 to 6.5 eV. X-ray diffraction confirms the partially ordered cubic crystal structure and the presence of ordered domains in the sample on the order of 15 nm in diameter. An oscillator model, with either one or two Tauc-Lorentz oscillators, was used to describe the interband transition in our spectra. Ellipsometry and transmission data show the direct band gap at 5.8 eV with an Urbach tail below, giving an onset of absorption at approximately 4.9 eV. The vibrational spectra was modeled using a nine factor Lyddane–Sachs–Teller model, where one factor shows a nonphysical switch in LO and TO positions with a negative amplitude, but was necessary to describe the line shape.

ACKNOWLEDGMENTS

This work was supported by the National Science Foundation (DMR-1104934 and DMR-1505172) and by the Army Research Office (W911NF-14-1-0072). The infrared ellipsometry measurements were carried out at the Center for Integrated Nanotechnologies, an Office of Science User Facility operated for the U.S. Department of Energy (DOE) Office of Science by Los Alamos National Laboratory (Contract No. DE-AC52-06NA25396) and Sandia National Laboratories (Contract No. DE-AC04-94AL85000). The work at the University of Fribourg was supported by the Schweizerische Nationalfonds (SNF) through Grant No. 200020-153660.

- ¹P. Granger, V. I. Parvulescu, S. Kaliaguine, and W. Prellier, *Perovskites and Related Mixed Oxides: Concepts and Applications* (Wiley, Chichester, 2016).
- ²C. J. Fennie and K. M. Rabe, *Phys. Rev. Lett.* **97**, 267602 (2006).
- ³B. J. Gibbons and S. Trolrier-McKinstry, *IEEE Trans. Appl. Supercond.* **7**, 2177 (1997).
- ⁴A. Kumar, N. J. Podraza, S. Deney, J. Li, L. W. Martin, Y.-H. Chu, R. Ramesh, R. W. Collins, and V. Gopalan, *Appl. Phys. Lett.* **92**, 231915 (2008).
- ⁵S. Kamba *et al.*, *Phys. Rev. B* **85**, 094435 (2012).
- ⁶A. OHara, T. N. Nunley, A. B. Posadas, S. Zollner, and A. A. Demkov, *J. Appl. Phys.* **116**, 213705 (2014).
- ⁷T. Kocourek *et al.*, *Appl. Phys. Lett.* **107**, 172906 (2015).
- ⁸C. M. Nelson, M. Spies, L. S. Abdallah, S. Zollner, Y. Xu, and H. Luo, *J. Vac. Sci. Technol., A* **30**, 061404 (2012).
- ⁹B. C. Chakoumakos, D. G. Schlom, M. Urbanik, and J. Luine, *J. Appl. Phys.* **83**, 1979 (1998).
- ¹⁰H. Li, L. Salamanca-Riba, R. Ramesh, and J. H. Scott, *J. Mater. Res.* **18**, 1698 (2003).
- ¹¹M. M. C. Chou, C. Chen, S. Y. Yang, C. H. Huang, and H. L. Huang, *J. Phys. Chem. Solids* **69**, 425 (2008).
- ¹²T. Runka, K. Lapsa, A. Lapinski, R. Alekseyko, M. Berkowski, and M. Drozdowski, *J. Mol. Struct.* **704**, 281 (2004).

- ¹³H. G. Tompkins and W. A. McGahan, *Spectroscopic Ellipsometry and Reflectometry: A Users Guide* (Wiley, New York, 1999).
- ¹⁴H. Fujiwara, *Spectroscopic Ellipsometry: Principles and Applications* (Wiley, Chichester, UK, 2007).
- ¹⁵H. G. Tompkins and E. A. Irene, *Handbook of Ellipsometry* (Springer, Heidelberg, 2005).
- ¹⁶H. G. Tompkins and J. N. Hilfiker, *Spectroscopic Ellipsometry: Practical Application to Thin Film Characterization* (Momentum, New York, 2015).
- ¹⁷K. Shimamura, H. Tabata, H. Takeda, V. V. Kochurikhin, and T. Fukuda, *J. Cryst. Growth* **194**, 209 (1998).
- ¹⁸B.-Q. Hu, X.-M. Wang, T. Zhou, Z.-Y. Zhao, X. Wu, and X.-L. Chen, *Chin. Phys. Lett.* **18**, 278 (2001).
- ¹⁹D. Nuzhnyy, J. Petzelt, S. Kamba, T. Yamada, M. Tyunina, A. K. Tagantsev, J. Levoska, and N. Setter, *J. Electroceram.* **22**, 297 (2009).
- ²⁰P. Marsik, K. Sen, J. Khmaladze, M. Yazdi-Rizi, B. P. P. Mallett, and C. Bernhard, *Appl. Phys. Lett.* **108**, 052901 (2016).
- ²¹T. Willett-Gies, E. DeLong, and S. Zollner, *Thin Solid Films* **571**, 620 (2014).
- ²²T. I. Willett-Gies, C. M. Nelson, L. S. Abdallah, and S. Zollner, *J. Vac. Sci. Technol., A* **33**, 061202 (2015).
- ²³C. Bernhard, J. Humlíček, and B. Keimer, *Thin Solid Films* **455–456**, 143 (2004).
- ²⁴A. Ghosh, C. M. Nelson, L. S. Abdallah, and S. Zollner, *J. Vac. Sci. Technol., A* **33**, 061203 (2015).
- ²⁵S. Zollner, J. G. Chen, E. Duda, T. Wetteroth, S. R. Wilson, and J. N. Hilfiker, *J. Appl. Phys.* **85**, 8353 (1999).
- ²⁶R. Tao, A. R. Guo, C.-S. Tu, I. Siny, R. S. Katiyar, R. Guo, and A. S. Bhalla, *Ferroelectr. Lett.* **21**, 79 (1996).
- ²⁷R. L. Andrews, “Probing the local structure of perovskites using Raman scattering spectroscopy,” M.S. thesis (The Ohio State University, 2012).
- ²⁸M. I. Alonso and K. Winer, *Phys. Rev. B* **39** 10056 (1989).
- ²⁹S. C. Tidrow *et al.*, *IEEE Trans. Appl. Supercond.* **7**, 1766 (1997).
- ³⁰D. J. Tao, H. X. Wu, X. D. Xu, R. S. Yan, F. Y. Liu, A. P. B. Sinha, X. P. Jiang, and H. L. Hu, *Opt. Mater.* **23**, 425 (2003).
- ³¹J. L. Servoin, Y. Luspain, and F. Gervais, *Phys. Rev. B* **22**, 5501 (1980).
- ³²M. V. Abrashev, A. P. Litvinchuk, M. N. Iliev, R. L. Meng, V. N. Popov, V. G. Ivanov, R. A. Chakalov, and C. Thomsen, *Phys. Rev. B* **59**, 4146 (1999).
- ³³P. Delugas, V. Fiorentini, and A. Filipetti, *Phys. Rev. B* **71**, 134302 (2005).
- ³⁴K. D. Fredrickson, C. Lin, S. Zollner, and A. A. Demkov, *Phys. Rev. B* **93**, 134301 (2016).